DISCLAIMER

Final Technical Report (FTR)

Cover Page

a. *Federal Agency*	Department of Energy	
b. *Award Number*	DE-EE0010191	
c. *Project Title*	Low-cost and high-performance heat exchangers for CSP	
d. *Recipient Organization*	University of Maryland, College Park	
e. *Project Period*	*Start:* 10/01/2022	*End:* 03/31/2025
f. *Principal Investigator (PI)*	Name: Ji-Cheng Zhao Title: Professor Email address: jczhao@umd.edu; jczhao@uconn.edu Phone number: 860-486-2221	
g. *Business Contact (BC)*	Name: Stephanie Swann Title: Assistant Director Email address: smbrack@umd.edu Phone number: 301-405-8079	
h. *Certifying Official (if different from the PI or BC)*	Name: N/A Title Email address Phone number	

Ji-Cheng Zhao *06/12/2025*

Signature of Certifying Official *Date*

By signing this report, I certify to the best of my knowledge and belief that the report is true, complete, and accurate. I am aware that any false, fictitious, or fraudulent information, misrepresentations, half-truths, or the omission of any material fact, may subject me to criminal, civil or administrative penalties for fraud, false statements, false claims or otherwise. (U.S. Code Title 18, Section 1001, Section 287 and Title 31, Sections 3729-3730). I further understand and agree that the information contained in this report are material to Federal agency's funding decisions and I have any ongoing responsibility to promptly update the report within the time frames stated in the terms and conditions of the above referenced Award, to ensure that my responses remain accurate and complete.

1. Acknowledgement:

"This material is based upon work supported by the U.S. Department of Energy's Office of Energy Efficiency and Renewable Energy (EERE) Solar Energy Technologies Office (SETO) under FOA-0002378 Award Number DE-EE0010191."

2. Disclaimer:

3. Executive Summary:

This project aimed to design and manufacture a low-cost and high-performance, particle–to–sCO_2 heat exchanger (HX) for Concentrated Solar Power (CSP) using additive manufacturing (AM). Three enabling technologies will be integrated to achieve the targeted cost and performance. The first technology is the extreme high-speed laser materials deposition (LMD) AM process known by its German acronym EHLA that was invented at the Fraunhofer Institute for Laser Technology [1-3]. The EHLA process utilizes a specially designed powder-feeding nozzle that enables a laser to melt the powder particles above the melt pool, in contrast to the conventional LMD process where the powders are melted inside the melt pool (**Fig. 1**). EHLA enables much faster deposition rate than conventional LMD without the need to wait for the powders to melt [1-3]. The second technology is an innovative double-helical HX geometry that can be easily fabricated using the EHLA process by rotating a rod at a high-speed to take advantage of the high EHLA deposition rate (**Fig. 2**). The double-helical fins separate the hot region (the hot particle side) and the cold region (the sCO_2 side) and provide large heat transfer surface area without a large pressure drop on the sCO_2 side. The particle side will have a larger gap to facilitate the particle flow. The outer rims of the double helixes can be sealed off using the same AM process, as shown in **Fig. 2**. After sealing-off, additional double helixes can be built radially on top of the first set to improve HX performance. The HX can be installed vertically for gravity-driven flow of the hot particles if necessary. The EHLA nozzle can be mounted on a robotic arm in future LMD AM processes to make very large parts; for instance it has been employed to coat the entire hydraulic cylinders, **Fig. 2(g)** and **2(h)**. Thus, the HX can be part of future CSP tower structures if desired.

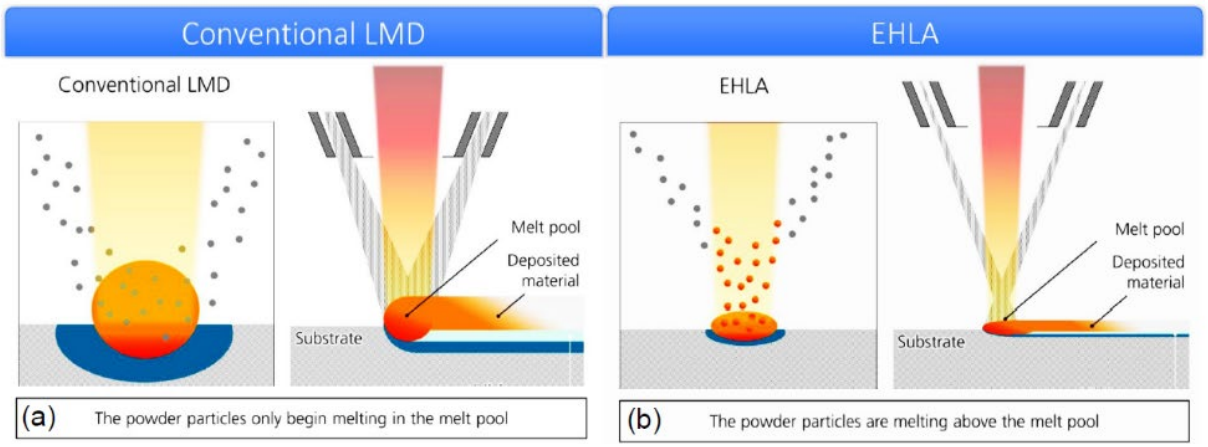

***Fig. 1**: Comparison of (a) conventional laser metal deposition (LMD) with (b) the new 100X faster EHLA process [1-2].*

The third technology is a low-cost high-temperature alumina-forming austenitic (AFA) steel TMA-6350 invented at the Oak Ridge National Laboratory (ORNL) that has creep and oxidation resistance up to 1100 °C [4,5].

These technologies together will enable high-performance and low-cost HXs for particle–to–sCO_2 for CSP. Wide implementation of the proposed HXs in the future will help reduce the HX cost, improve solar-to-electric efficiency, and thus reduce levelized cost of energy (LCOE) from CSP systems.

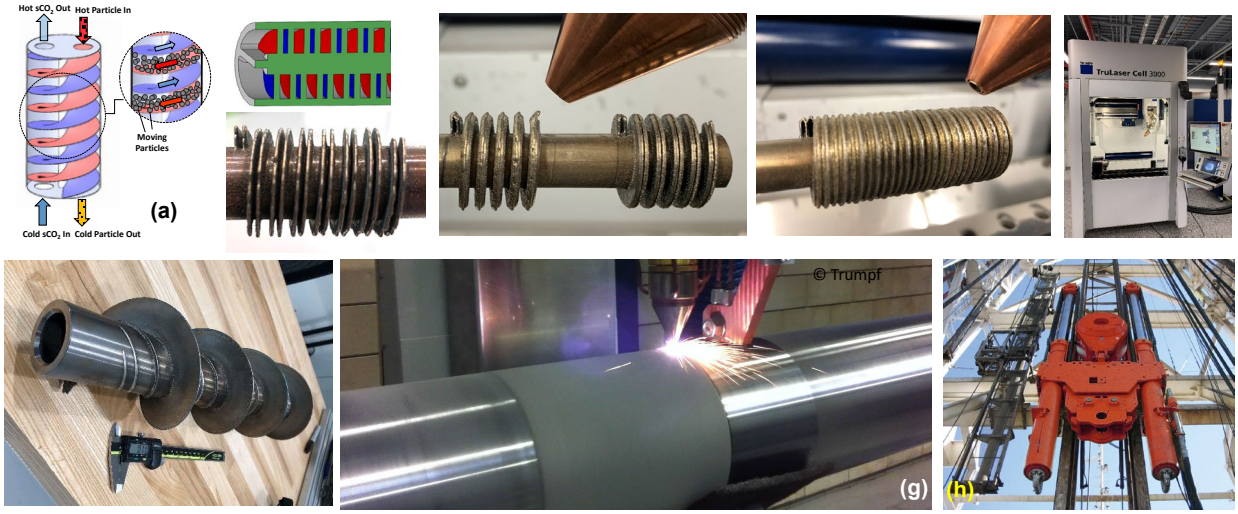

***Fig. 2**: Illustration of the proposed double-helical HX (a) using the EHLA-enabled AM process (It is also noted that the spacing between the helixes of the particle side will be larger than that in the sCO_2 side). Photos in (b) to (d) show the double helixes before, during and after the tip seal-off by tilting the nozzle 45° (both left and right). Photo in (e) shows the TruLaser 3000 system at UMD that is 9 feet tall with a very large build chamber. Photo in (f) shows a large helical part built using the TruLaser 3000 system. Photos in (g) and (h) show the capability of coating very large parts such as hydraulic cylinders by mounting EHLA-nozzle on a robotic arm.*

4. Background:

Particle-based CSP has received high level of attention in recent years as it allows a higher operating temperature (>700 °C vs. ~600 °C for salt-based systems), greater solar-to-electric efficiency and lower costs as compared to conventional liquid-based systems. Employment of particle-based systems will improve electricity production by 8% and reduce LCOE by 10.8% in comparison with the existing molten salt plants [6,7]. The solar-to-electric efficiency in CSP plants also directly depends on the particle-to-sCO_2 temperature drop across the power-cycle's primary HX. In fact, for every additional 10 °C temperature drop across the HX, the efficiency is reduced by 0.5% [8]. This necessitates development of high effectiveness (> 90%) particle-to-sCO_2 HXs for CSP. Heat transfer in such HXs is primarily limited by the particle side. In fact, the thermal resistance on the particle side can be 9 times higher than that of the CO_2 side [8]. Due to the clogging issue associated with complex HX geometries, most existing particle-to-sCO_2 HX designs have been limited to simple vertical or horizontal straight tubes or channels with low convective heat transfer coefficients. On the CO_2 side, the very high operating pressure and temperature necessitate robust and sturdy channel designs such as those in printed circuit heat exchangers (PCHE) which require diffusion bonding. Due to low value of heat transfer coefficients, high transfer effectiveness can only be realized by increasing the heat transfer surface area, leading to larger sizes that increase the HX cost and impeding the attainment of the DOE's 2030 cost targets of $0.05/ kWhr LCOE. Achieving this target requires development of HXs with cost < $100/kWth [8] which is a major challenge for existing technologies.

Our proposed HXs can address the above issues by introducing centripetal force in the flow to enhance heat transfer on both sides. The cold and hot flow travel in two separate helical paths in a counter flow arrangement, **Fig. 2(a)**. This configuration is very effective for heat exchange because of its large heat transfer area in a small space with a high heat transfer coefficient. In the proposed design the particles flow in one helical path while sCO_2 flows in an opposite direction. The particles are in contact with the heat transfer surface, which is an advantage over fluidized beds that have reduced particle contact times [9,10]. The helical angle of the HX can be used as a design parameter to control the speed of moving particles and their residence time, and an optimum double helical design is expected to be achieved.

As part of the progress towards the CSP 2030 LCOE goals, next generation high-heat-transfer-coefficient particle–to–sCO_2 HXs appropriate for Generation 3 CSP systems are critically needed as clearly stated in the SETO FOA DE-FOA-0002378. Our proposed project will impact manufacturing and cost of HXs for CSP systems and beyond. It will advance reliable AM for CSP.

The proposed technology will significantly impact HX manufacturing, including: (1) developing fast and reliable AM of high-performance HXs at a cost comparable to existing mass-production processes, which will positively affect not only the targeted CSP sCO_2 HXs, but also other power generation applications; (2) enabling the manufacturing of robust and high-performance components out of a low-cost and high-capability alloy, and thus helping introduce a novel alloy (TMA-6350) for CSP applications and other energy systems of extreme operating conditions; and (3) enabling 3D printing of very large HXs

since LMD-based AM systems can make very large components that most currently available powder-bed metal AM systems cannot.

The most impact of our project will be on the reduction of the HX cost and maturation of a new AM technology. DOE's 2030 cost targets of $0.05/kWhr LCOE requires the development of HXs with a cost < $100/kWth [8]. This project will achieve such a low cost through integration of three technologies: the EHLA AM process, the new high-efficiency HX design that can be fabricated at a high speed, and the low-cost steel TMA-6350. Since there is no need for the EHLA process to wait for the injected powders to melt (already melted in contrast to the case of LMD), the travel speed of the deposition can be increased up to 200 meters/minute without sacrificing the quality of the deposits. This results in a deposition rate (e.g., 1.5 kg/hour) up to 100 times higher than conventional LMD [1-3]. In addition, since the powders are melted inside the laser beam, much less powder is ejected in comparison with LMD, thus the EHLA process can achieve high powder utilization efficiency in contrast to the conventional LMD. This further reduces the manufacturing cost. The high deposition rate will have the biggest cost impact, leading to at least 50% reduction of the AM cost since the machine build/use time accounts towards more than 50% of the AM processing cost [12]. By increasing the build speed by dozens of times, the build-time can be shortened substantially.

The novel double-helical HX design, consisting of counter-flowing hot particles and cold sCO_2 fluid passages whirling around one another, is projected to offer significant performance advantages with negligible increase in pressure drop [11]. The compact size also reduce the AM build time and alloy powder consumption. The ORNL AFA steel TMA-6350 [4,5] consists mostly Fe and 35 wt.% Ni and low concentrations of other elements, thus it is very low cost. The low cost of the double-helical HXs is a robust step towards reaching the SETO 2030 CSP price targets.

5. Project Objectives:

The main objective of this R&D is to design, manufacture and hydro test a low-cost and high-performance, particle–to–sCO_2 double helix heat exchanger (HX) for CSP using high-speed additive manufacturing (AM) and a cost-effective yet high-performance alloy, aiming at helping reduce the overall cost of levelized cost of electricity (LCOE) of CSP.

We have developed a simulation code to model the HX thermal performance for a given set of geometrical parameters (helical surface angle and thickness, channel gaps, total length, etc.) and operating conditions (such as fluid flow rate, system pressure, and particle flow rate). We have input the 3D printing constraints into our modeling tool to design a 20 kW HX unit. Structural FEM has been performed on the HX to meet the pressure requirements on the sCO_2 side using the mechanical property values of a high strength alloy. We have iterated the design to conform to the structural requirements with the best effort to satisfy the pressure vessel code.

One key feature of this project is to test the suitability of an alumina-forming austenitic (AFA) steel developed by the Oak Ridge National Laboratory (ORNL). The AFA alloy has the advantage of good high-temperature, superior oxidation resistance, and low cost; thus ideally suited for the HXs for CSP. Yet, this AFA still has not been tested for potential CSP HX applications. As a matter of fact, no powders for AM have ever been atomized

for this alloy, to the best of our knowledge. AM experience of this alloy would accelerate its application in HXs and other components.

We have performed high-speed laser material deposition processing parameter sweeping for the AFA alloy to determine the optimum 3D print settings and determined the fabrication constraints. Metallographic examination was performed on samples produced during the parameter sweeping to examine the level of porosity and cracks (if any) to provide feedback to identify the optimal 3D printing settings. Coupons made using these optimal settings were found to be crack-free with very low porosity levels, indicating the good printability of this AFA alloy.

This project is funded in the category of Small Innovative Projects in Solar (SIPS) and thus is exploratory in nature. Our approach integrated high-speed AM, novel double helix design, and a low-cost yet high-performance alloy capable of operating at high temperatures. The research outcome will contribute to the reduction of LCOE of CSP.

6. Project Results and Discussion:

Task 1.1 Heat exchanger design:

As part of this effort, a theoretical model for performance evaluation of the heat exchanger was developed. The heat exchanger that was developed under the current effort is a double–helix geometry (**Fig. 3**). In this geometry, the hot particles enter through a feed hopper from the top and are driven downward through a helical path by gravitational force. On the other hand, the cold sCO_2 enters from the bottom and moves upward in a separate helical path in a counterflow arrangement. During this process, heat is transferred from the hot particles to the cold sCO_2. The goal is to determine the heat exchanger size that can meet the performance requirements.

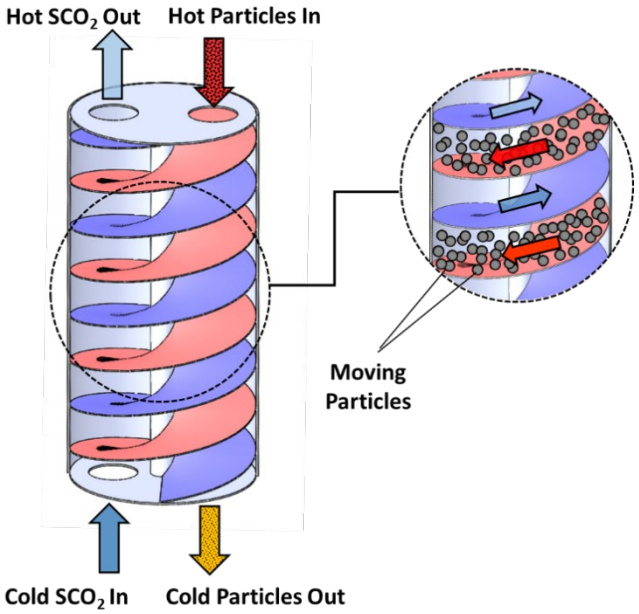

Fig. 3: Moving packed-bed particle-to-sCO_2 double helix heat exchanger.

The design requirements for the heat exchanger are presented in Table 1. These requirements were established based on a literature review and input from experts.

***Table 1**: The design requirements for the 20kW heat exchangers*

Metric	Value	Unit
Thermal Duty	20	kW_t
Design Pressure	20	MPa
sCO2 Operating Pressure	17	MPa
Particle Inlet Temperature	625	°C
Particle Outlet Temperature	< 570	°C
sCO2 Inlet Temperature	400	°C
sCO2 outlet Temperature	> 550	°C
Particle flow rate	120-200	g/s
sCO2 Flow Rate	100	g/s

The thermophysical properties of sCO_2 and a selected type of particle are given in Tables 2 and 3, respectively. Air properties are shown in Table 4.

***Table 2**: Thermophysical properties of sCO_2 at P = 17 MPa and T = 480 °C*

Property	Value	Unit
Density, ρ	116.9	Kg/m3
Specific Heat, C_p	1220	J/kg-K
Thermal conductivity, k	0.0573	W/m-K
Viscosity, μ	35.1E-6	Pa-s

***Table 3**: CARBO HSP 40/70 sintered bauxite particles [13]*

Property	Value	Unit
Particle Density, ρ_s	3300	Kg/m3
Specific Heat, $C_{p,s}$	148.2 $T_s^{0.3093}$	J/kg-K
Particle Thermal conductivity, k_s	2	W/m-K
Flowing Volume fraction, $\emptyset_{s,f}$	0.55	
Packed volume fraction, $\emptyset_{s,p}$	0.60	
Mass-median particle diameter	320	μm

***Table 4**: Thermophysical properties of air at P = 1 bar and T = 555 °C*

Property	Value	Unit
Air Density, ρ_g	0.42	Kg/m^3
Air Specific Heat, $C_{p,g}$	1105	J/kg-K
Air conductivity, k_g	0.0586	W/m-K
Viscosity, μ_g	37.2E-6	Pa-s

The heat exchanger performance can be characterized based on the overall heat transfer coefficient (U), which can be calculated as follows:

$$Q = UA \cdot \Delta T_{lm} \tag{1}$$

where Q is the heat exchanger heat duty, *A* is the heat transfer area, and ΔT_{lm} (LMTD) is the log mean temperature defined by Eq. (2).

$$\Delta T_{lm} = \frac{\left(T_{s,out} - T_{sCO2,in}\right) - \left(T_{s,in} - T_{sCO2,out}\right)}{\ln\left(\frac{\left(T_{s,out} - T_{sCO2,in}\right)}{\left(T_{s,in} - T_{sCO2,out}\right)}\right)} \tag{2}$$

The heat transfer Area, *A*, for a helical surface is calculated from Eqs. (3), (4) and (5) where N_{turns} is the number of helical turns, S_{pitch} is the pitch length, R_o is the outer radius, and R_i is the inner radius.

$$A_2 = N_{turns} / 2 \cdot \left(R_o \cdot \sqrt{4 \cdot \pi^2 \cdot R_o^{\,2} + S_{pitch}^{\,2}} + \frac{S_{pitch}^{\,2}}{2 \cdot \pi} \cdot ln\left(2 \cdot \pi \cdot R_o / S_{pitch} + \sqrt{\left(1 + 4 \cdot \pi^2 \cdot \frac{R_o^{\,2}}{S_{pitch}^{\,2}} \right)} \right) \right) \tag{3}$$

$$A_1 = N_{turns} / 2 \cdot \left(R_i \cdot \sqrt{4 \cdot \pi^2 \cdot R_i^{\,2} + S_{pitch}^{\,2}} + \frac{S_{pitch}^{\,2}}{2 \cdot \pi} \cdot ln\left(2 \cdot \pi \cdot R_i / S_{pitch} + \sqrt{\left(1 + 4 \cdot \pi^2 \cdot \frac{R_i^{\,2}}{S_{pitch}^{\,2}} \right)} \right) \right) \tag{4}$$

$$A = 2(A_2 - A_1) \tag{5}$$

The overall heat transfer coefficient (U) is related to the convective heat transfer coefficients on the particle and sCO2 sides and the conductive conductance of the helical surface as given in Eq. (6).

$$\frac{1}{U} = \left(\frac{1}{h_{s,w}} + R_C^{"} + \frac{t_{HX}}{k_{HX}} + \frac{1}{h_{sCO2,w}}\right) \tag{6}$$

There are different correlations for the heat transfer coefficient in helical channels. In our calculations, we used the Mandal and Nigam correlation given by Equation (7) [14].

$$Nu_{sCO2,w} = \frac{h_{sCO2,w} d_{h,sCO2}}{k} = 0.55\, De^{0.637} Pr^{0.4} \tag{7}$$

The Dean and Reynolds numbers are given as

$$De_{sCO2} = Re_{sCO2} \sqrt{d_{h,s\,CO2}/D_{avg}} \tag{8}$$

$$Re_{sCO2} = \frac{\dot{m}_{sCO2} d_{h,sCO2}}{\mu (R_o - R_i) H_{sCO2}} \tag{9}$$

where

$$d_{h,sCO2} = \frac{2(R_o - R_i) H_{sCO2}}{(R_o - R_i) + H_{sCO2}} \tag{10}$$

and

$$D_{avg} = (R_o + R_i) \tag{11}$$

Calculating the heat transfer coefficient on the particle side is inherently complex due to the thermal interactions among discrete particles during flow and the influence of the helical flow path they follow. Since no established correlation for this specific flow configuration has been identified in the open literature, a correlation developed for straight channels has been employed as a first-order approximation, as shown in Eq. (11).

$$Nu_s = \frac{h_{s,w} d_{h,s}}{k_{s,eff}} = \left(\left(\frac{1.128}{\sqrt{L^*}} \right)^2 + 9.87^2 \right)^{\frac{1}{2}} \tag{12}$$

where

$$L^* = \frac{L}{d_{h,s}\, \mathrm{Pe_{d_h}}} \tag{13}$$

and

$$L = N_{turns} \sqrt{\left((\pi D_{avg})^2 + S_{pitch}^2 \right)}$$
$$d_{h,s} = \frac{2(R_o - R_i) H_s}{(R_o - R_i) + H_s} \tag{14}$$

The Péclet number is defined as

$$\mathrm{Pe}_{\mathrm{d_h}} = \frac{u d_{h,s}}{\alpha_{s,eff}} \tag{15}$$

where the particle velocity is calculated as

$$u = \frac{\dot{m}_s}{\emptyset_{s,f}\rho_s(R_o - R_i)H_s} \tag{16}$$

$$\emptyset_{g,f} = 1 - \emptyset_{s,f} \tag{17}$$

And the thermal diffusion coefficient is calculated from Eqs. (17)-(20).

$$\alpha_{s,eff} = \frac{k_{s,eff}}{\rho_{eff}C_{p.s}} = \frac{k_g}{(1-\emptyset_{g,f})\rho_s C_{p,s}}\left(\emptyset_{g,f} + \frac{\beta(1-\emptyset_{g,f})}{\gamma\frac{k_g}{k_s}+\epsilon}\right) \tag{18}$$

Where $\beta = 0.895$ and $\gamma = 0.666$

$$\epsilon = \begin{cases} \epsilon_1 & when\ \emptyset_{g,f} < 0.260 \\ \epsilon_2 + (\epsilon_1 - \epsilon_2)\dfrac{(\emptyset_{g,f} - 0.26)}{0.216} & when\ 0.260 \le \emptyset_{g,f} \le 0.476 \\ \epsilon_2 & when\ 0.476 < \emptyset_{g,f} \end{cases} \tag{19}$$

$$\epsilon_1 = \frac{0.352\left(\dfrac{\frac{k_s}{k_g}-1}{\frac{k_s}{k_g}}\right)^2}{\ln\left(\frac{k_s}{k_g} - 0.545\left(\frac{k_s}{k_g}-1\right)\right) - 0.455\left(\dfrac{\frac{k_s}{k_g}-1}{\frac{k_s}{k_g}}\right)} - \frac{2k_g}{3k_s} \tag{20}$$

$$\epsilon_2 = \frac{0.072\left(\dfrac{\frac{k_s}{k_g}-1}{\frac{k_s}{k_g}}\right)^2}{\ln\left(\frac{k_s}{k_g} - 0.925\left(\frac{k_s}{k_g}-1\right)\right) - 0.075\left(\dfrac{\frac{k_s}{k_g}-1}{\frac{k_s}{k_g}}\right)} - \frac{2k_g}{3k_s} \tag{21}$$

When designing the heat exchanger, several critical factors must be addressed to ensure optimal thermal performance, structural integrity, and efficient operation:

- **Particle-side gap:** The gap must be wide enough to permit unobstructed particle flow, while avoiding excessive width that would reduce the heat transfer coefficient.
- **Helical surface inclination:** The angle should be sufficiently steep to enable gravity-driven particle movement along the surface.
- **Surface wall thickness:** The wall must be thick enough to withstand the pressure differential between supercritical CO_2 and the ambient environment; however, overly thick walls can impair heat transfer performance.
- **sCO_2 pressure drop:** The pressure drop on the supercritical CO_2 side should remain within acceptable limits to maintain overall system efficiency.

To calculate the particle velocity and the Péclet number, knowing the mass flow rate of the particles is necessary. However, the particle mass flow rate remains unknown and depends on several factors, including the helix angle (surface inclination angle), channel gap, surface finish, and other parameters. This relationship is complex and must be determined experimentally. In the design of the heat exchanger, the helical structure can be divided by intermediate walls positioned between the inner shaft, around which the helical surfaces are constructed, and the outer wall of the heat exchanger. This configuration creates a multi-stack system, where the total channel width (Ro−Ri) is divided into (Ro−Ri)/n, with n representing the number of stacks. Although this design does not provide significant advantages in thermal performance, it allows for a reduction in the thickness of the helical wall separating the sCO_2 side from the particle side by offering mechanical support through the addition of intermediate walls. Figure 2 illustrates a 3-stack double helix heat exchanger design.

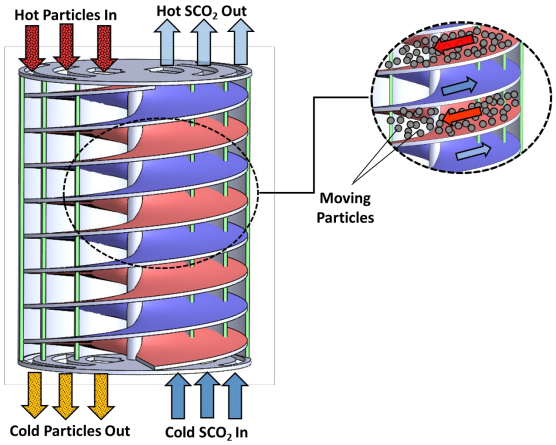

***Fig. 4**: Particle-to-sCO_2 multi-stack double helix heat exchanger*

In addition to the multi-stack structure, the heat exchanger can also be designed with multiple parallel passes, providing parallel flow paths for particles at the same helix angle. The advantage of this design is that it enables higher inclination angles and increased particle mass flow rates within a given volume. **Fig. 5** illustrates a 3-pass design.

Table 5: Input Parameters

Parameter	Value	Unit
Total Heat Duty, Q	20	kW
Hot side mass flow rate, $\dot{m}_s$	0.150	Kg/s
cold side mass flow rate, $\dot{m}_{sCo2}$	0.120	Kg/s
Hot side inlet temperature, $T_{s,in}$	625	^{o}C
Cold side inlet temperature, $T_{sCo2,in}$	400	^{o}C
Inner radius of helical surface, R_i	9.5	mm
Channel Gap on cold side, H_{sCO2}	5	mm
Number of Helical Turns, N_{turns}	20 or 30	
Wall thickness, t_{wall}	1.5	mm
Number of parallel passes, $N_{parallel}$	4	
Effective Thermal Conductivity of particle flow, $k_{s,eff}$	0.25	W/mK
Effective Thermal Conductivity of particle flow near wall, $k_{s,eff,\ nw}$	0.16	W/mK

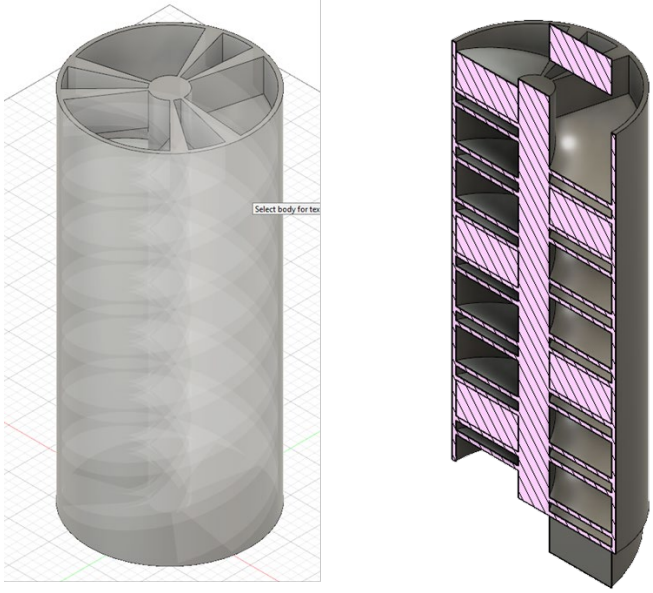

***Fig. 5**: Particle-to-sCO$_2$ three-pass double helix heat exchanger*

As part of this effort, we conducted modeling of the helical heat exchanger, assuming a quadruple-pass design with four passages, respectively, for the flow of particles and sCO2. Our primary objective was to explore the influence of the hot-side channel gap on the heat exchanger's performance. Table 5 summarizes the input parameters used in this study.

Figs. 6 to 5 present the findings from this parametric study. It is important to highlight that in these calculations, we assumed a particle mass flow rate of 150 g/s. However, it is crucial to emphasize that the confirmation of such a flow rate can only be obtained through flowability experiments.

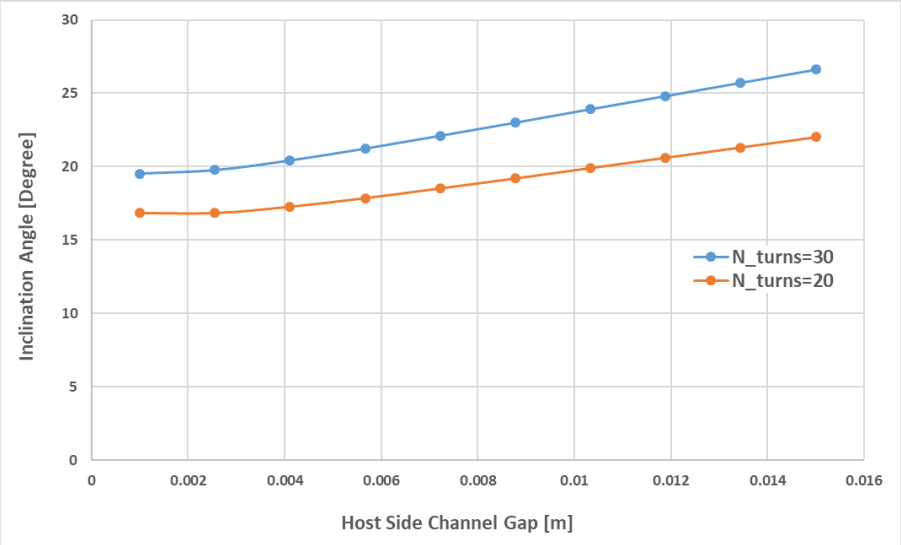

***Fig. 6**: Variation of the helix inclination angle with hot-side channel gap for two different numbers of turns, N_{turn} = 20 and 30*

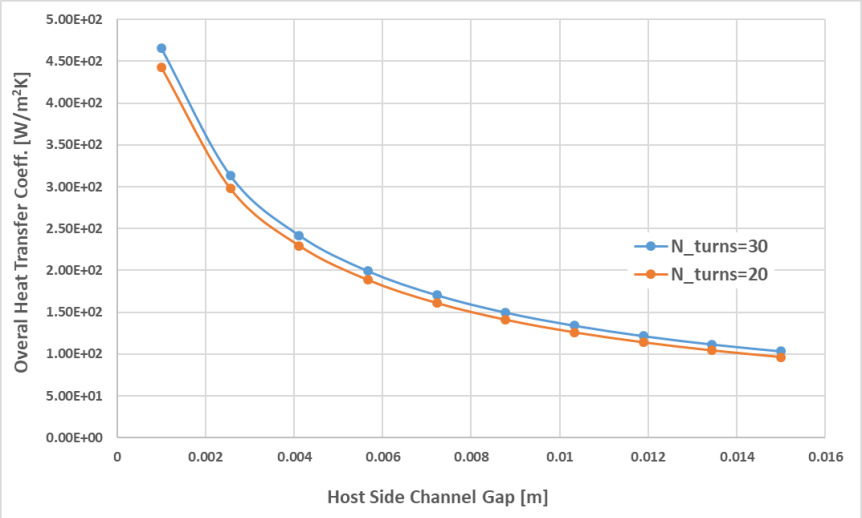

***Fig. 7**: Variation of the overall heat transfer coefficient with hot-side channel gap for two different numbers of turns, N_{turn} = 20 and 30*

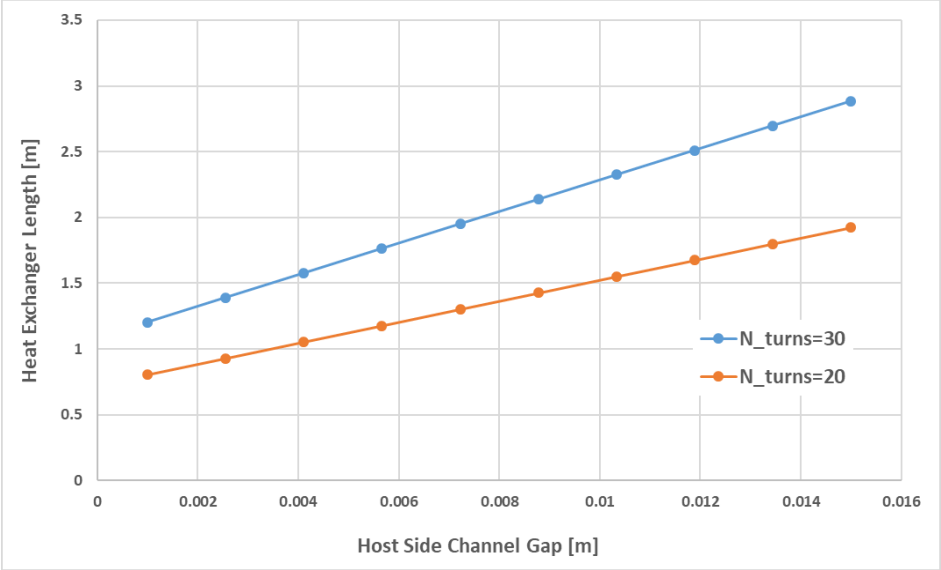

Fig. 8: Variation of the heat exchanger length with hot-side channel gap for two different numbers of turns, N_{turn} = 20 and 30

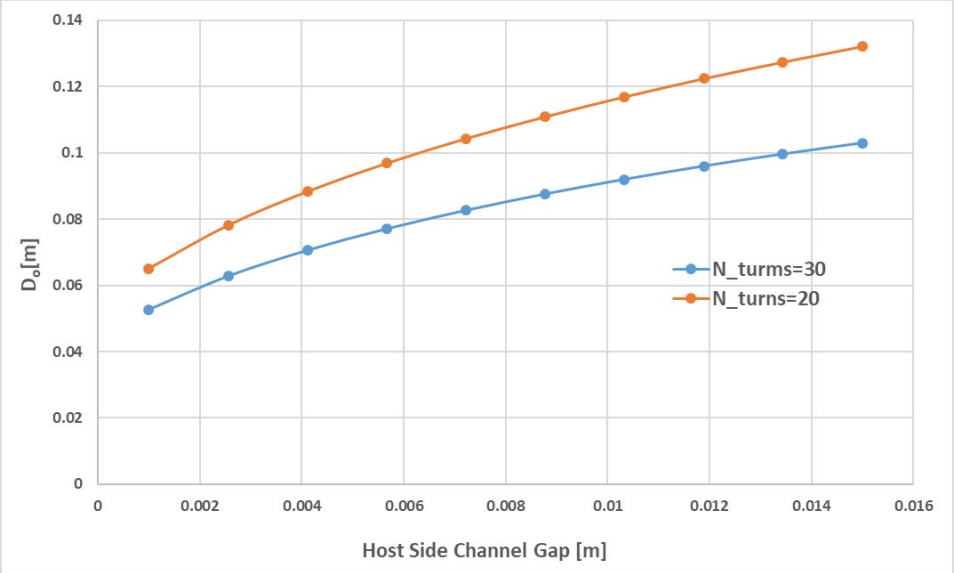

Fig. 9: Variation of the heat exchanger diameter with hot-side channel gap for two different numbers of turns, N_{turn} = 20 and 30

Based on the outcomes of this modeling effort, the following observations can be deduced:

- Tests show that a steep inclination angle is essential for achieving the targeted particle flow rate.
- Simulations reveal that when the channel gap on the particle side exceeds 12 mm, an inclination angle of more than 20° is attainable.

- Wider channel gaps on the particle side result in a decreased heat transfer coefficient and an expansive heat transfer surface.
- Such an expansive surface necessitates a heat exchanger of over 1.5 m in length and a diameter surpassing 100 mm.
- By adding more parallel passes, the heat exchanger can be made both shorter and more compact, without compromising the angle of inclination.

Task 1.3 Particle flow test:

Our team has performed numerous particle flow tests using the oxide particles that are being used in the CSP systems. To make the tests cost effective and also to cover wide range of geometries and parameters, we extensively used 3D printed plastic models first and then tested the results on the 3D printed metal prototypes.

Utilizing the particle flow measurement setups built at our lab over the duration of this project, a series of nozzle-based tests were performed to address the parameters outlined in the project proposal. We originally proposed testing parameters in helixes and specified channel gap and channel angle as two of the primary parameters. Flow nozzles are preferable for testing angles as the angle of a helix gets shallower with increasing radius – angled nozzles enable isolated testing of this parameter. Additionally, by separating channel gap from the other parameters which it typically drives, such as helix pitch, we can more clearly understand how it effects flow. Finally, while we didn't specify channel width testing in the proposal it is our final core geometric parameter and should be considered given that helixes get shallower with increased radius.

The channel angles we have selected are 10, 25, and 40 degrees. The channel gap was specified in the proposal as 5-10x particle diameter, the median diameter for the CARBOHSP 40/70 is 0.35mm while the maximum diameter is 0.6mm. Combining these and approximating to get a consistent set of steps we get 1.5mm, 3.0mm and 6.0mm as our channel gaps to test. For channel width we selected values 20mm and 5mm to test the extremes.

Investigations into particle flow testing explored several different important parameters of the particles and helix structure. We found that the CarboHSP 40/70 particles would start flowing on a 3D printed metal plate between 20° and 25°. We also made use of easier to test circular tubing to determine a 1" tube at 30° could flow at 110 g/s and a 1" diameter helix at 40° could flow at 80 g/s. Helixes with rectangular cross sections, closer to what can be produced with metal additive manufacturing, were used to test additional parameters. One of the significant challenges for particle flow was identified with these rectangular helixes: the angle of the channel is steepest on the inner radius and significantly shallower at the outer radius. A rectangular helix with a 0.75" tall and 1.5" wide cross section and mid-helix angle of 30° was observed to flow at 101 g/s. Due to the relatively steep angle needed for powder flow, a multi-double helix structure was adopted: Multiple repeating copies of CO_2 and powder channels would enable significant area of contact for heat exchange while still allowing for powder flow. Multiple tests were performed including printed prototypes of 2x, 3x, 4x, and 8x 'pass'/'stack' designs.

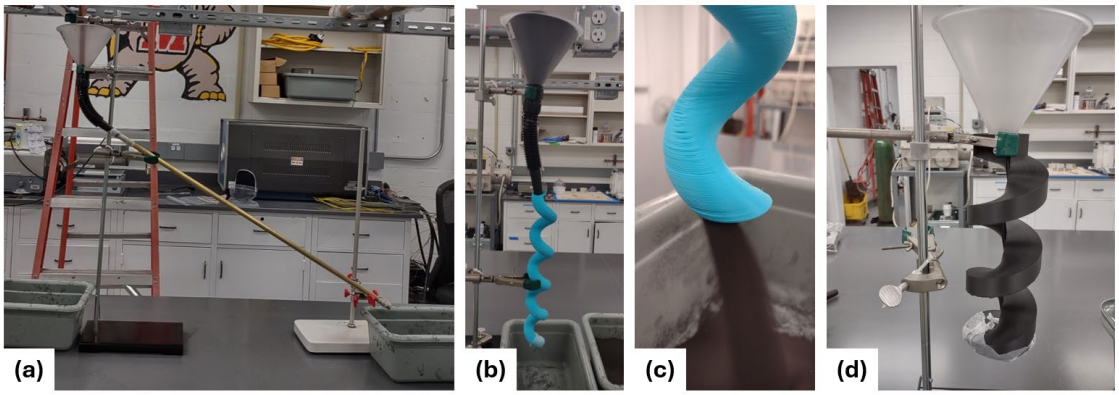

***Fig. 10**: Preliminary flow testing rigs. (a) Angled circular tube. (b,c) Circular helix before and during flow. (d) Rectangular helix.*

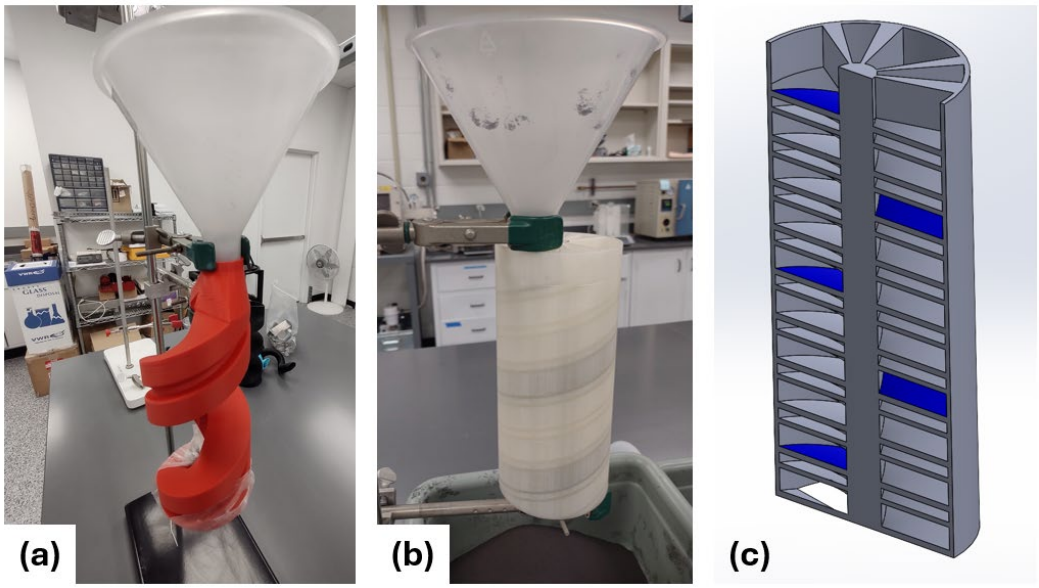

***Fig. 11**: Initial double helix designs (a) First "multi-pass" design with two particle channels around one CO_2 channel. (b,c) 4x double helix design shown in testing rig and in cross-section.*

Preliminary elevated temperature testing was carried out by placing a particle-filled stainless-steel tube inside a tube furnace with both tilted at 30° and then heating it to 300°C and 500°C before opening the end of the tube and allowing particles to flow. This was performed for both 5/8" and 1/2" tubes which exhibited ~41% and ~42% reduction in flowrate at 500°C vs room temperature respectively.

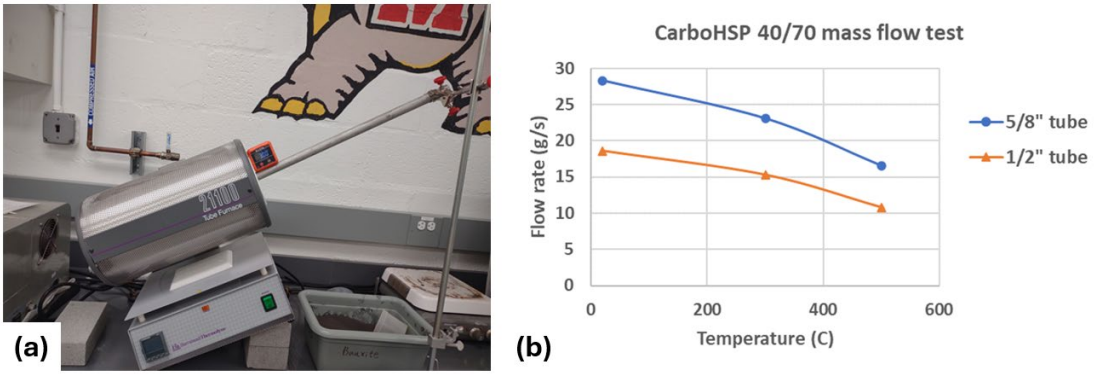

***Fig. 12**: High temperature flow testing. (a) Testing rig showing stainless-steel tube going through a tube furnace with both at an angle. (b) Results from temperature testing showing ~41% and ~42% decrease in flowrate at 500°C versus room temperature for 5/8" and 1/2" tubes respectively.*

Following our preliminary investigations, we started development of a load cell & Arduino based experimental rig for more robust quantitative data collection. We 3D printed a set of nozzles for baseline data collection and testing of the load cell-based data collection system. The nozzles included a small circular cross section, a down-facing rectangular cross section, and two side-facing rectangular cross sections, one with a gentle curve and the other with a flat floor.

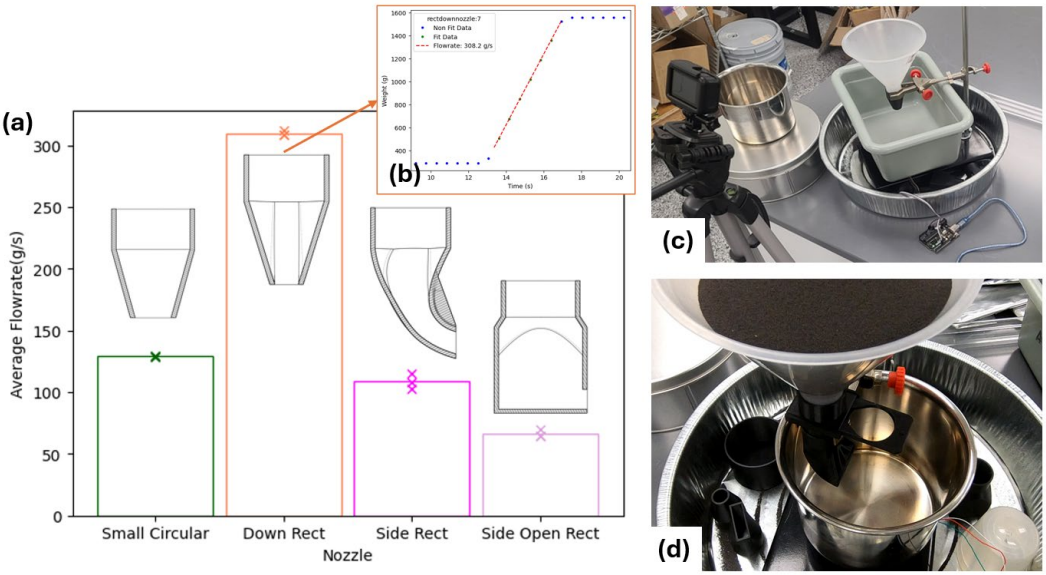

***Fig. 13**: Load cell testing (a) Quantitative results from load cell-based flow measurement for the small circular, down-facing rectangular, side-facing curved rectangular, and side-facing flat rectangular nozzles. (b) Illustrative example of the data collected by the measurement system with linear fitting on the steady state flow plotted. (c,d) Pictures of the experimental setup showing a funnel feeding into the nozzles and then into a container with the load cell below that.*

We 3D printed two 7x double helix mock-up channels for testing with the load-cell system. One was printed as half of a helix loop, the other as a full loop. These designs suggested the full 7x double helix would exhibit a flowrate exceeding 300g/s at room temperature.

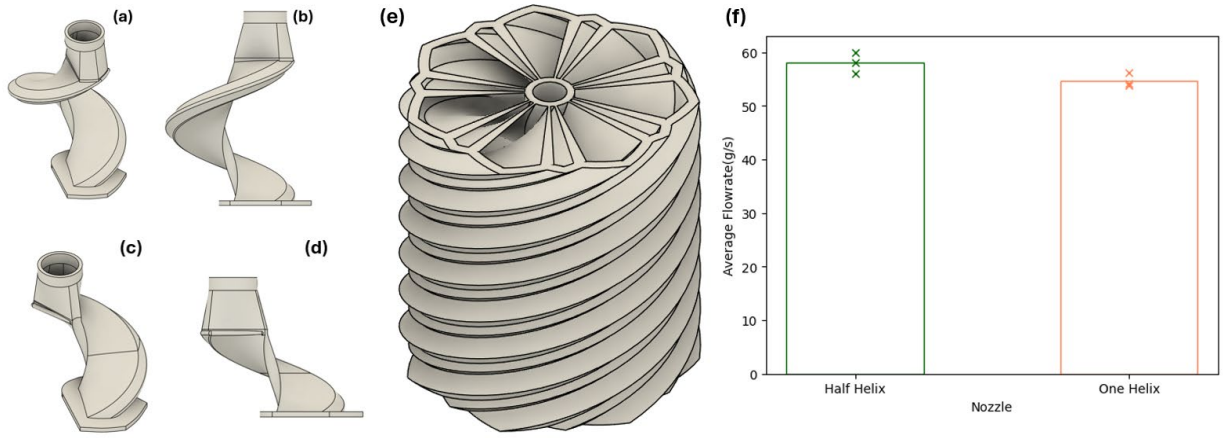

***Fig. 14**: 7x double helix mock-up (a,b) CAD model for the full-loop helix that was tested. (c,d) CAD model for the half-loop helix that was tested. (e) CAD model of what the full 7x double helix would look like. (f) Results from three flow tests of each helix that suggest the full 7x double helix could exceed 350g/s flowrate.*

We began isolated parameter testing by polymer 3D printing modular particle flow nozzles at varying channel width, channel gap (the channel dimensions perpendicular to the floor/the flow direction), and channel angle as well as nozzle extenders to test the aforementioned parameters over longer flow distances. It was observed that the channel gap had a significant positive correlation with the flowrate per area. It was also observed that while extremely narrow channels significantly limit flow/area, there is not a significant impact on flow/area for channels that are much wider. The effect of channel angle on flowrate/area was also determined to have an approximately sinusoidal fit. The nozzle extenders provided additional clarity to the previously observed measurement of flow angles. At a 40° angle the flowrate stayed nearly constant with increasing distance up to the maximum tested distance of 250mm while at a 25° angle the flowrate slowly decreased until no longer flowing at 150mm. As the previous tests were done on very short segments of material, we believe this result is reasonable. We would expect the angle for continuous flow to be slightly steeper than 25°.

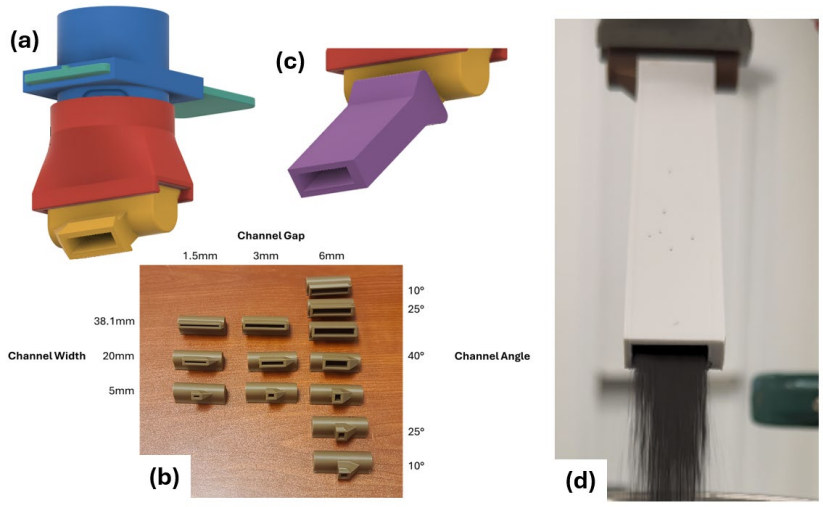

***Fig. 15**: Nozzle-based parameter investigation. (a) CAD model of testing assembly showing slide gate, mount, and nozzle. (b) Picture of multiple nozzles that were used showing the different channel widths, channel gaps, and channel angles tested. (c) CAD model showing extender attached to nozzle assembly. (d) Picture showing particles flowing from the end of one of the nozzle extensions.*

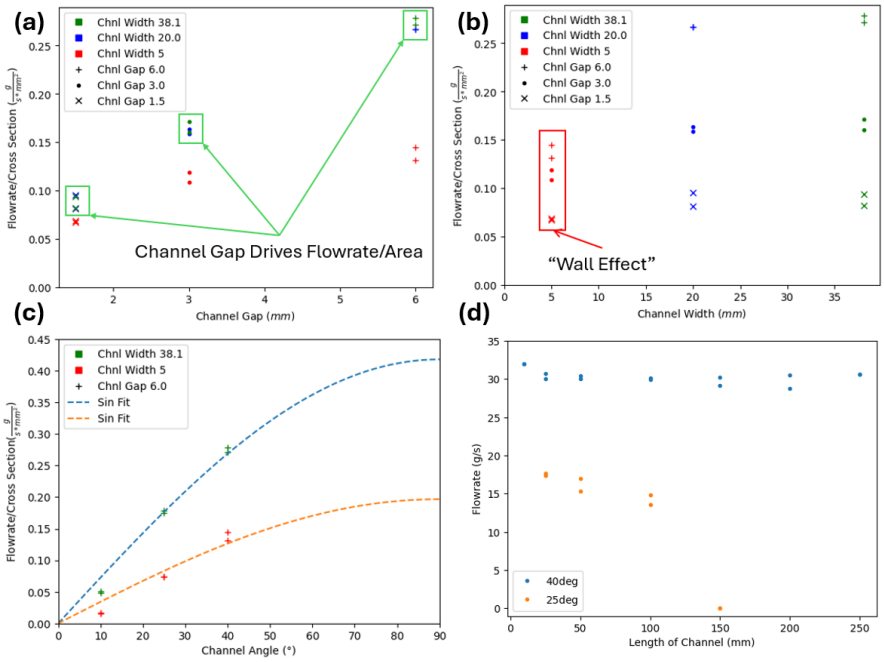

***Fig. 16**: Quantitative parameter investigation results. (a) Flowrate/area vs channel gap showing that channel gap has a strong positive correlation with flowrate/area (b) Flowrate/area vs channel width showing that extremely small channels have reduced flow ("Wall Effect") but for wider channels width has a limited positive correlation with flowrate/area. (c) Flowrate/area vs channel angle showing that three angles tested can be approximately fitted by a sine function. (d) Flowrate vs length of channel for 40° and 25° channels showing that for 40° there is no significant decrease in flow with increasing distance while for 25° the flow full stops by a length of 150mm.*

We also printed an "open face" helix that allowed us to more clearly visualize what was happening inside the helix structure during particle flow. This experiment was very significant as it revealed some of the major differences between nozzle and helix behavior. The beginning of the helix flows almost identical to a nozzle and because gravity accelerates the down-helix particles away from the beginning it acts as one of the primary bottlenecks to flow. However, the remainder of the helix behaves very differently, the shallow outside slope results in particle accumulation at the outside and the steep inside results in particles moving too quickly to stay on the inner radii. This result suggested to us that reducing channel width could significantly improve performance as it would reduce or eliminate the shallowest outer radii and could also allow for a shallower inner radius which would ensure that the entire helix has particles flowing through it. We also believe reducing the channel gap would help to restrict the fastest moving particles, by causing them to bounce against the ceiling of the channel, such that the inner radius would not be devoid of particles.

This parameter-focused testing allowed us to develop a prototype for Nozzle Informed Helix Prediction. This technique discretizes the helix radii, calculates flow behavior for each radial slice based on the parameters that were fit from the nozzle parameter testing, and then sums the flow of each radii to give an estimate for the flow at the very beginning of the helix structure. This prediction approach showed decent alignment with the half and full loop helixes that had been previously printed. Because it predicted slightly higher than measured values, we used this prediction technique as an upper bound for flowrate performance, any designs which were not predicted to reach our performance goals using this would almost certainly not be viable and could be eliminated.

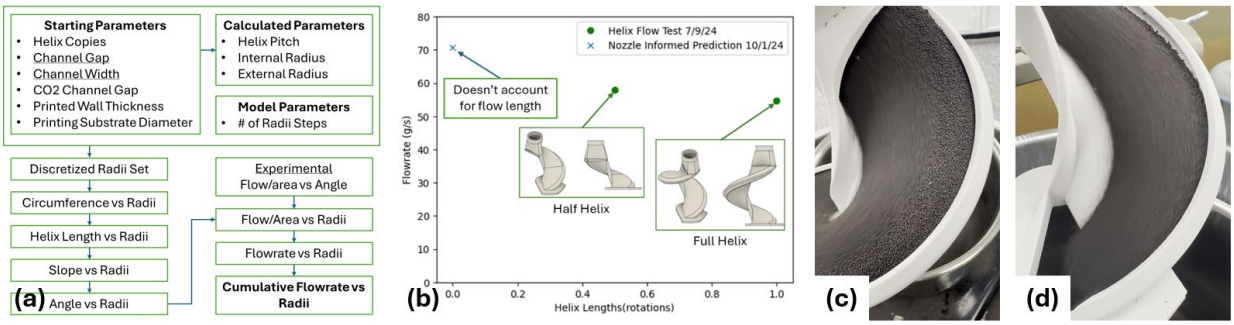

***Fig. 17**: Helix Optimization, prediction, and open-face helix observations. (a) Process flow for Nozzle Informed Helix Prediction (b) Comparison plot of half and full helix flow tests with the nozzle informed prediction showing reasonable alignment. (c) Open-face helix channel near the top showing 'nozzle-like' flow as well as stagnation at the outer radii. (d) Open-face helix channel near the bottom showing unique 'helix-like' flow with depletion at the inner radii.*

We 3D printed a final HX polymer prototype and tested it in single channel & 8x channel configurations. We also fabricated a metal printed single helix and tested it with flow from both the top and bottom openings. These results showed that the polymer mock-up was a good approximation of the metal channel and slightly under-performed it which suggests that a full metal HX would outperform the full 8x polymer HX that we were able to test. The 4 single channels that were tested in the 8x polymer mockup had an average flowrate

of 34.5g/s for an effective 276g/s predicted flowrate. The full 8x polymer HX when tested all together, had an average flowrate of 284g/s, outperforming the prediction from the single channels. The metal single channel had an average flowrate of 36.6g/s, slightly higher than the polymer average, resulting in an 8x prediction of 293g/s for a full metal HX. Given that the polymer single channel average under-predicted the polymer 8x channel average it is possible that we would also see higher performance from a full 8x metal HX. Factoring in our previously measured ~40% flowrate reduction at 500°C, we could expect that a full 8x metal HX could flow around ~175g/s at 500°C significantly exceeding our target flowrate.

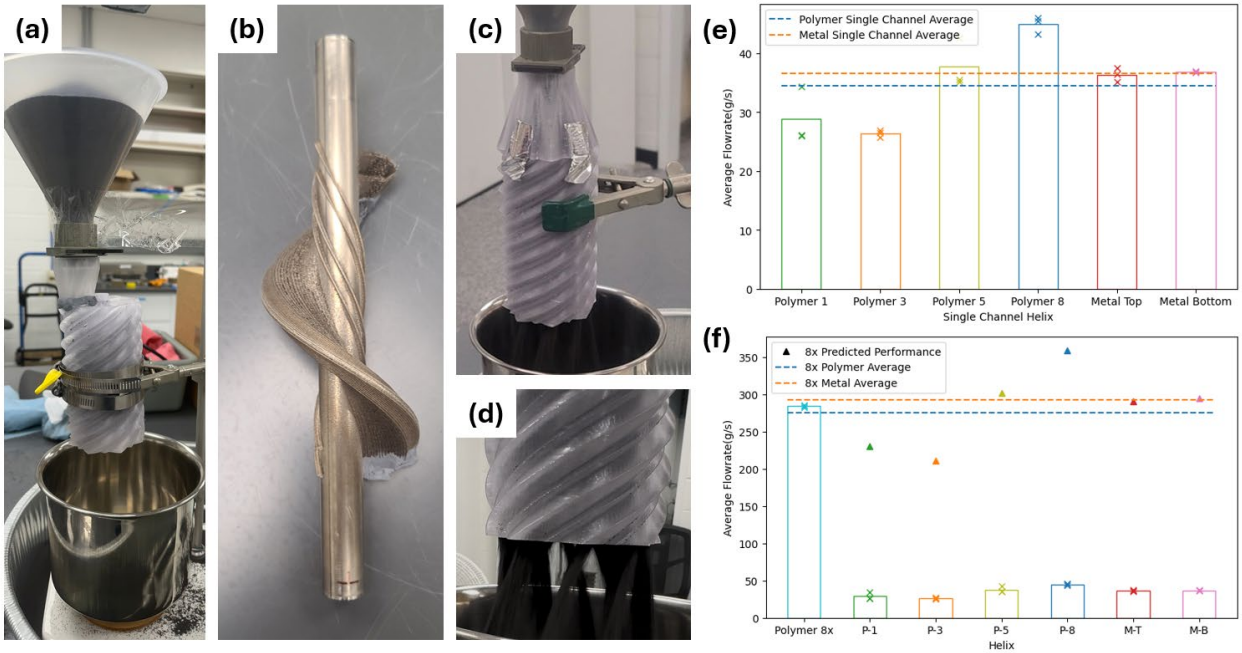

***Fig. 18**: Final particle flow results. (a) Polymer 8x double helix mock-up with single channel testing nozzle. (b) Metal printed single channel used for testing. (c,d) Polymer 8x double helix mock-up with all-channel testing nozzle before and during testing. (e) Comparison of the 4 polymer single channels tested with the two metal channel orientations tested showing overall similarity of performance. (f) Comparison of the polymer 8x with the single channels as well as their individual 8x predicted performance and the average 8x predicted performance.*

Task 1.4 HX prototype fabrication:

One hundred (100) pounds of the ORNL AFA alloy powder was purchased and received from Powder Alloy Corporation. About 40 pounds was in the correct particle size range for our machine after sieving, which should be sufficient to complete the project. Initial parameter testing began once the powder was loaded into the machine. The first test was a single line speed ramp from 1500 to 3000 mm/min at a set power of 300 watts. This was followed by a power ramp test from 200 to 350 watts at a set speed of 2000 mm/min. The lines shown in **Fig. 19** were visually inspected, and with no obvious issues in the parameter space, the values of 2000 mm/min and 300 watts were chosen.

***Fig. 19**: Single line speed ramp (top) and power ramp (bottom).*

Single and triple line walls were printed next with an assumed layer height based on a similar material. These walls were then cut from the plate (**Fig. 20**), mounted in resin, and polished for inspection.

The mounted samples were first viewed under an optical microscope. The stitched images are shown below in **Fig. 21**. The samples are mostly dense, however there is some porosity. This indicates that while the operating parameters are close, more work is needed to optimize the settings for a fully dense wall.

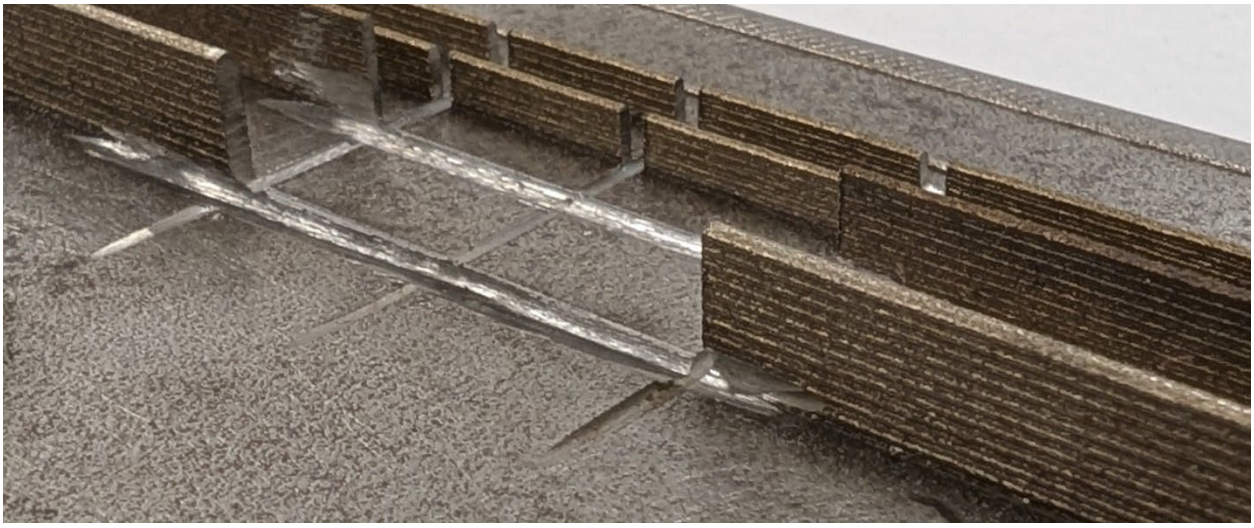

***Fig. 20**: Triple line wall (front) and single line walls (back).*

Fig. 21: *Triple line walls (left) and single line walls (right).*

Images of the samples were also taken by SEM as seen in **Fig. 22**. Results clearly shows crack-free AM builds with very low porosity level – even lower than the regular melting and casting samples/components.

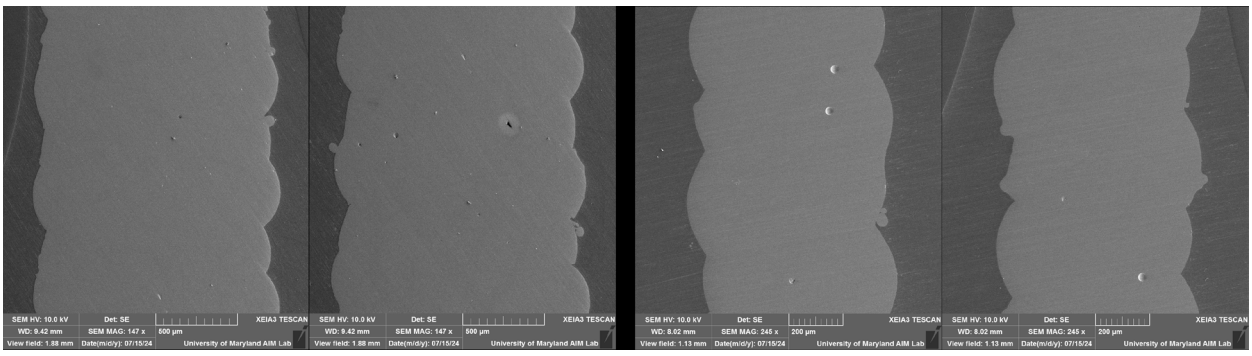

Fig. 22*: Triple line walls (left) and single line walls (right).*

The layer height was found to be incorrect after measuring the built walls, so another series of builds followed (**Fig. 23**). After each run the wall height was measured and compared to the expected height. The difference in layer height was then added to the next programmed layer height until the expected and actual heights agreed.

***Fig. 23**: Triple line walls to find layer height.*

A single helix version of the final design was printed with some success. The channel was completed in the 3D printing run, however a very rough and uneven surface was produced as seen in **Fig. 24**. As the channel was built up, the walls began to thin out in the higher portions. This did not leave enough base material for the next layer to bond with, leading to over-melting of the edges as well as additional overspray from the partially melted particles.

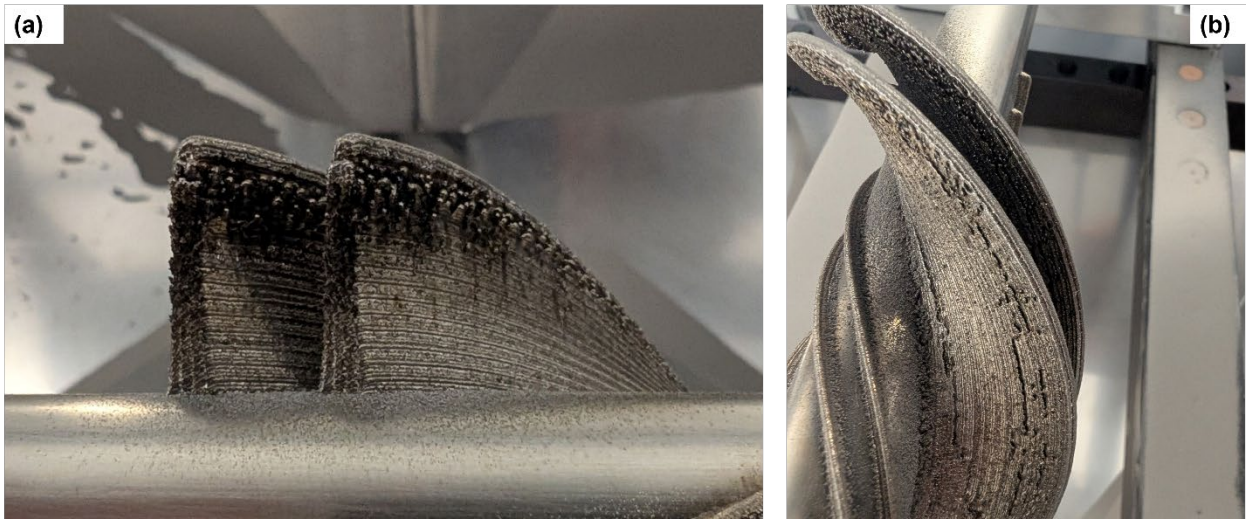

***Fig. 24**: Over-melting on the ends (a) and along the length of the helix (b).*

The same build strategy was used to attempt the full 8x design (**Fig. 25**). Unfortunately, this build failed early due to more variance in the base build-rod, as well as the additional heat input from multiple channels. The build was stopped before the variance in wall height from one side to the other became large enough to cause a collision with the printer head.

***Fig. 25**: Over-melting on 8x print.*

A new build strategy was developed to address the challenge of printing tall and high aspect ratio walls. Instead of leaving the head in a vertical position for all paths, the nozzle was pointed into the center of the wall by 10° for the outermost pass. This

ensured that the whole melt pool was always pointed into previous layers, and it significantly improved the surface finish and consistency of the wall as seen in **Fig. 26**.

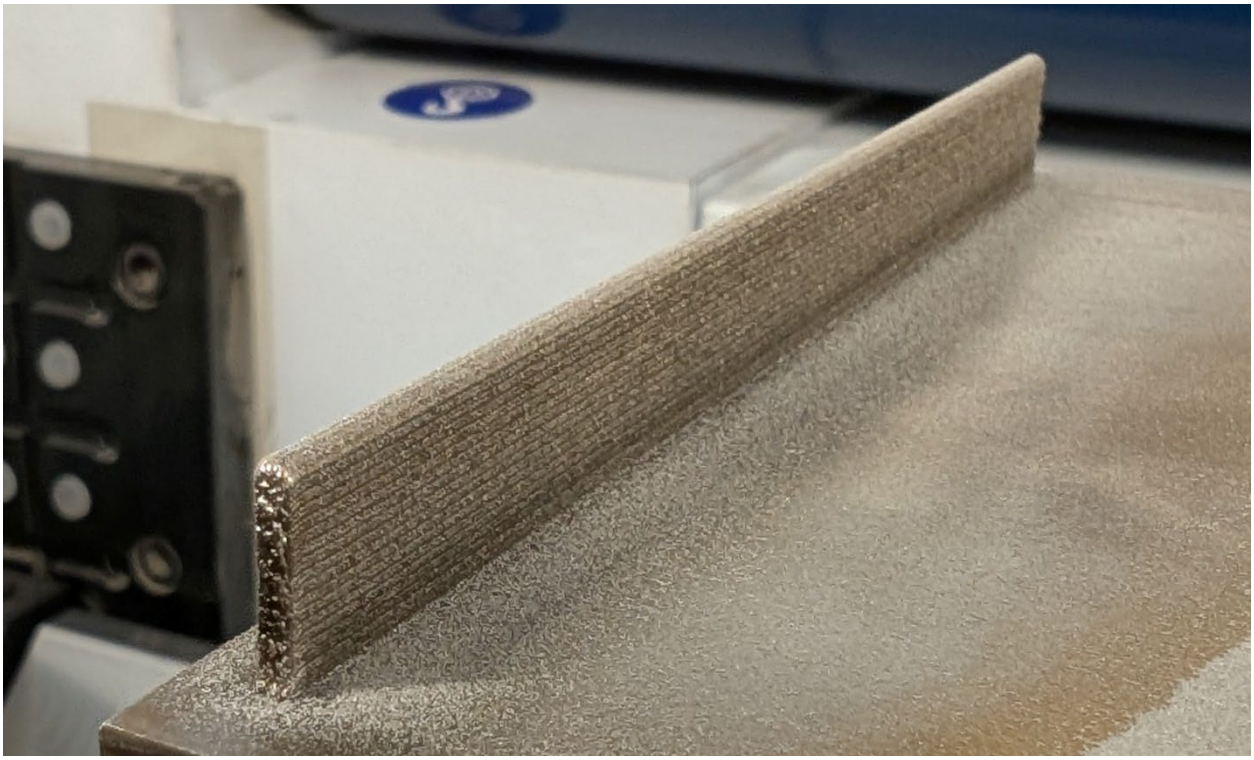

***Fig. 26**: Test wall for angled outside paths.*

While this adjustment was relatively trivial for the 2D wall test, it presented a larger challenge to implement for the helical geometry. The build path changes for every layer as the helix is built out radially, and requires a new 5-axis transformation to be computed. The printer in its current configuration is calibrated for the B-axis transformation, which allows it to compensate for the X-axis and Z-axis movements needed to maintain a position with a given B-axis value. However, to maintain the same relative angle on the helix wall, additional C-axis rotation and YZ-axis translation were needed as seen in **Fig. 27**.

The updated path proved to be successful for the next single helix trial seen in **Fig. 28**. There were no signs of over-melting, and the surface finish was much smoother. The channel was also successfully closed out over the entire length.

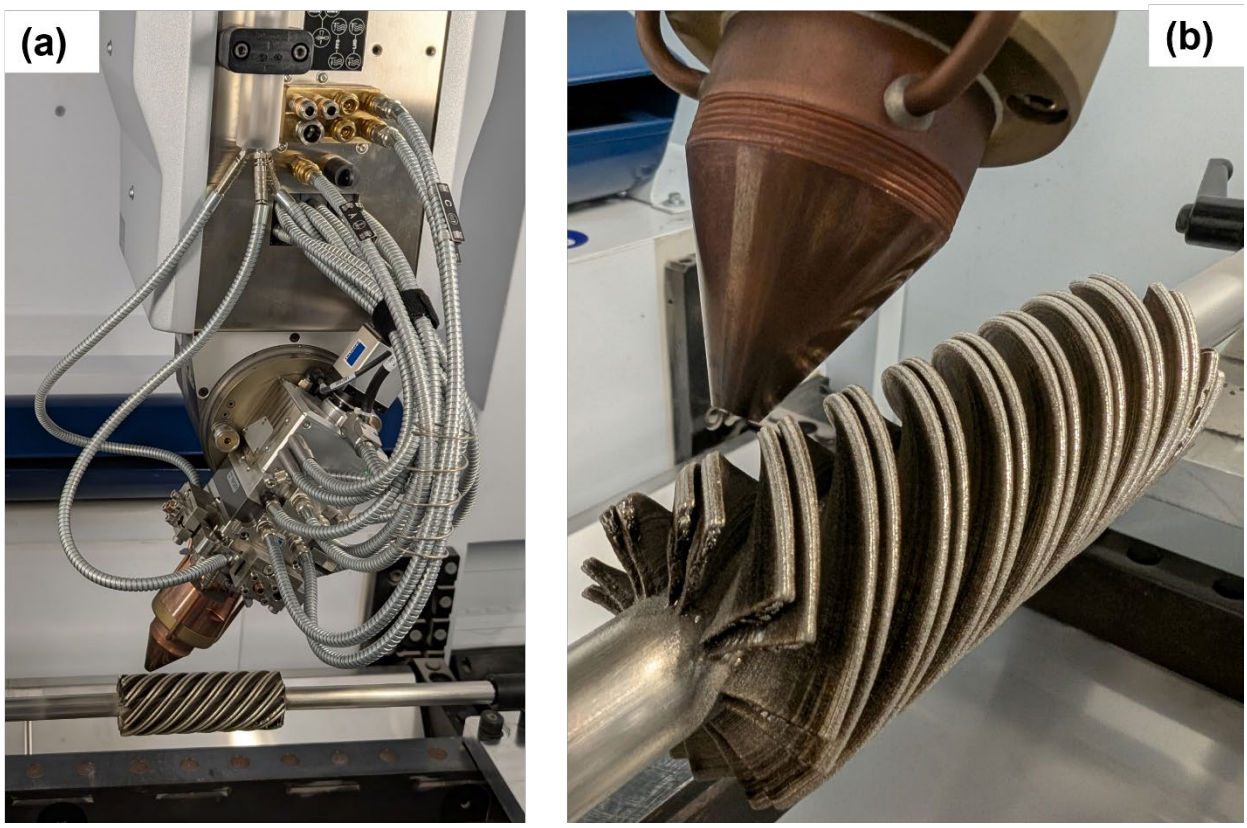

***Fig. 27**: Transformation for angled paths. (a) B-axis rotation and Z-axis translation. (b) A-axis rotation and Y-axis translation.*

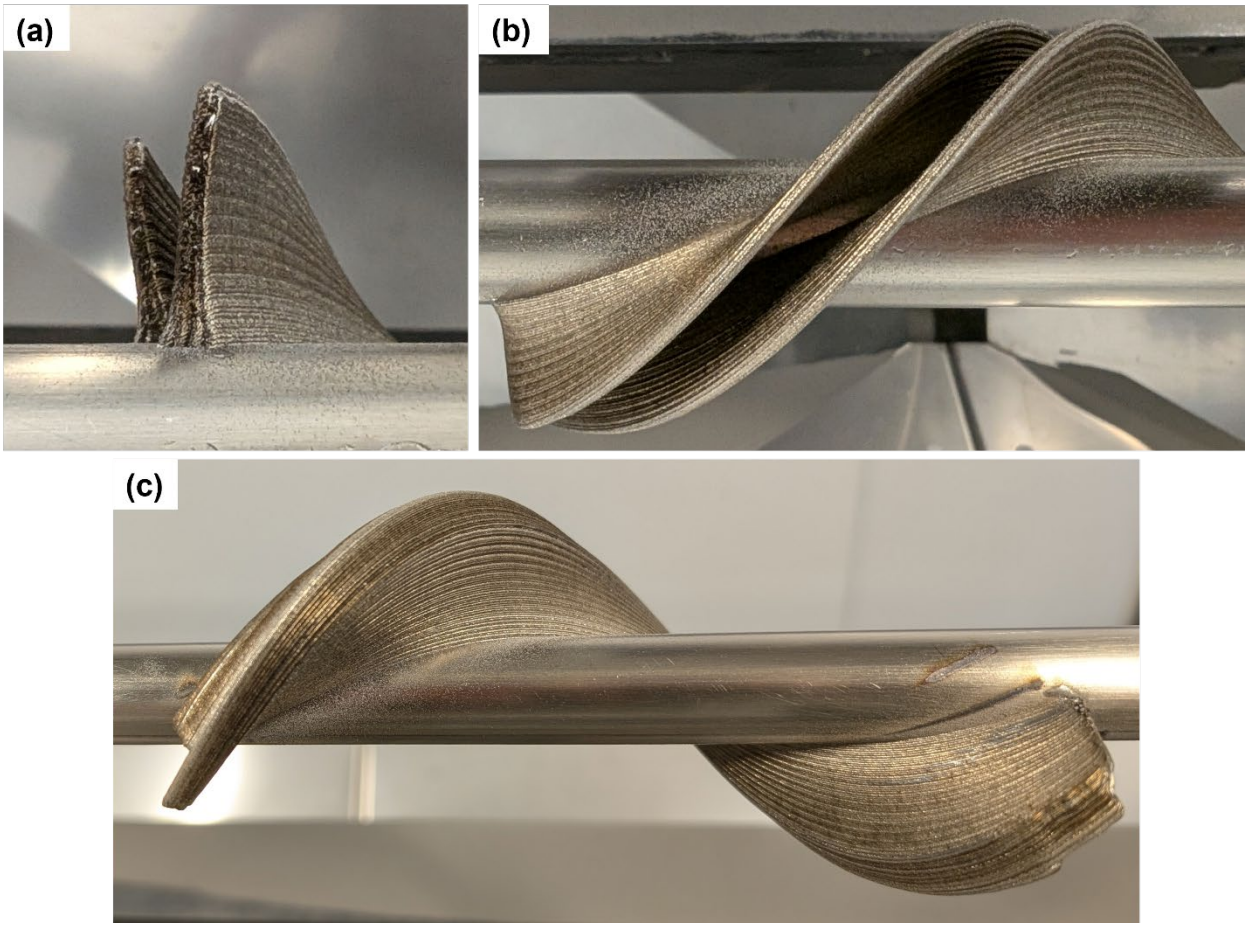

***Fig. 28**: Single helix with updated pathing. (a) Wall ends. (b) Wall length. (c) Closed channel.*

Finally, the full 8x design was printed again with the updated strategy (**Fig. 29**). There were issues again related to the base rod, but the wall heights remained within a manageable variance. However, more errors arose as the build transitioned to the angled walls to close out the channels. The differences in wall heights allowed for some of the angled sections to build perfectly, and others to miss some at the base layer. These variances and voids get larger and larger every subsequent layer due to the continued over-melting (**Fig. 30**). It is also noted that the unconstrained side of the build is lower quality than the constrained side. Future work is needed to compensate for the thermal differences between different points of the build.

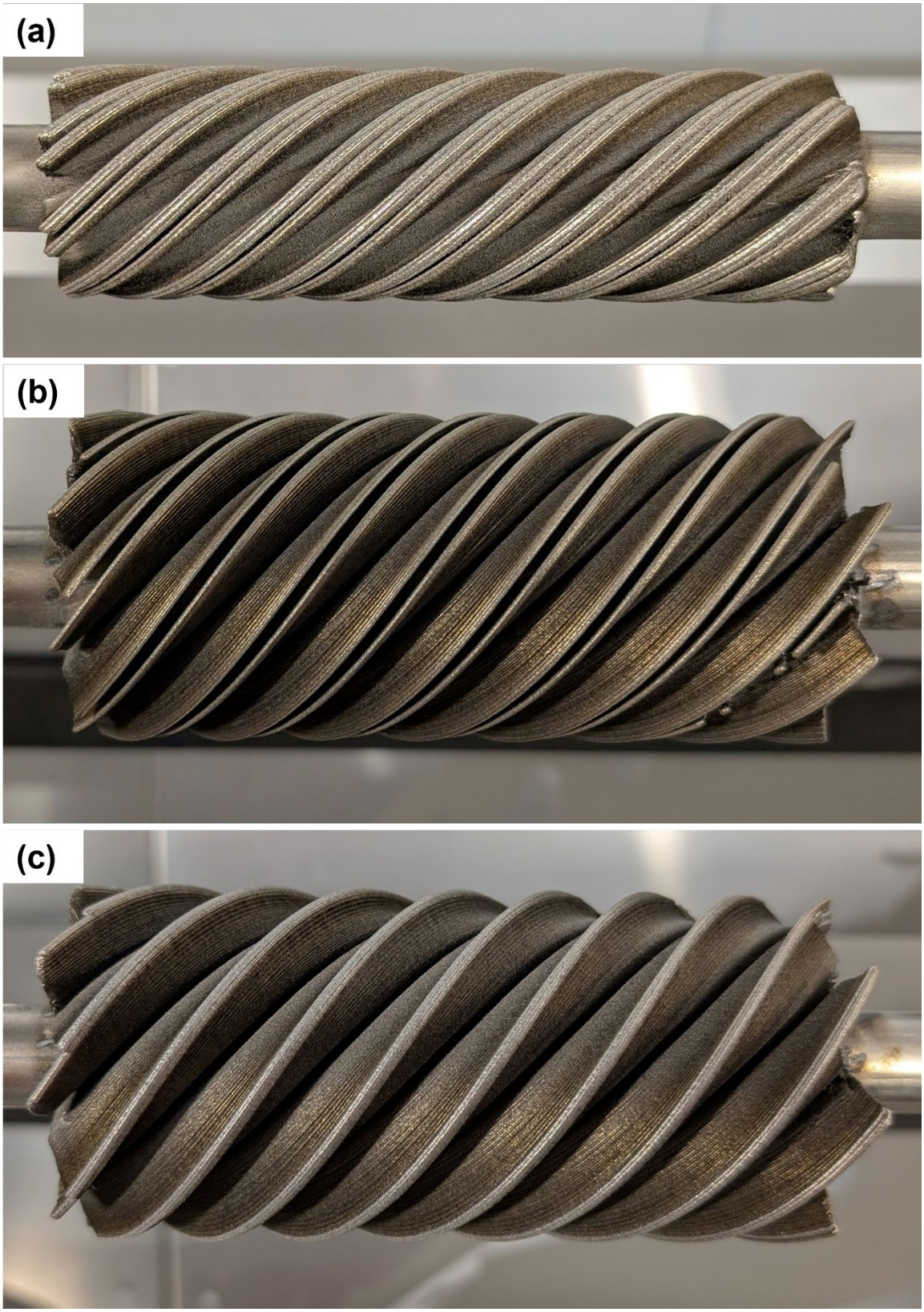

***Fig. 29**: 8x build progress. (a) Vertical section. (b) Angled section. (c) Closed out channels.*

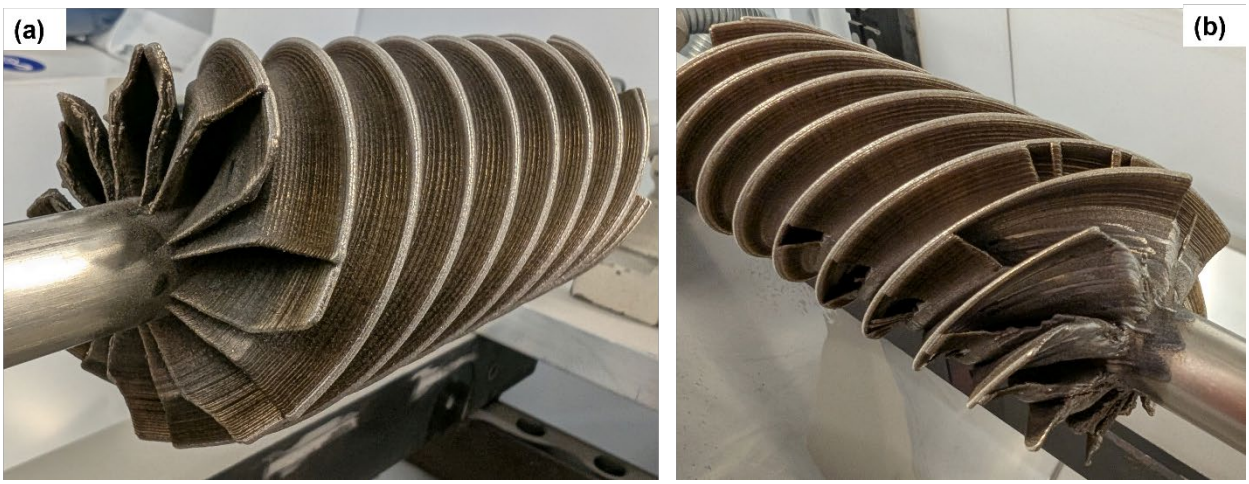

***Fig. 30**: 8x build errors. (a) Constrained side. (b) Free side.*

Even though we did not obtain a completely sealed HX from one end to the other of the HX prototype shown in **Fig. 30** due to the complexity of the geometry of the HX that required a more advanced 3D printing software package to design and implement the 3D printer head motion. It is completely viable in real industrial settings where such advanced 5-axis motions are commonplace. Our project cannot afford such a software package, especially at the end of this project when the 8x fully compact HX was built.

7. Significant Accomplishments and Conclusions:

- Our team has designed a particle-to-sCO_2 HX with a double-helix architecture that will be much more efficient than the state-of-the-art vertical-plate based HXs for CSP.
- We tested the oxide particle flow rate under various tilt angles and gap/spacings and identified the minimum angle of 20° and the minimum gap of 12 mm for uninterrupted flow of oxide particles without an applied pressure to push the oxide particles through the HX – the information will be useful to guide further non-vertical-plate particle-to-fluid HXs.
- We ordered and purchased AM powders of the AFA alloy developed by ORNL and demonstrated its excellent printability during AM and thus opened up this high-temperature-capable and cost-effective alloy for future CSP applications and beyond.
- There were heavy backlogs in several powder-making vendors as a result of high interest in AM and the limited capacity of making AM powders of new alloys (Most vendor did not want to stop their atomizers from making existing alloys for sale). Due to the very long duration in obtaining the AM powders of the ORNL AFA alloy after placing the purchase order, we were unable to perform the mechanical property measurements on samples made with AM; however, we have full confidence that the AM-printed samples will have good properties based on the crack-free and low-porosity characteristics.

- We demonstrated the capability of the high-speed TruLaser 3000 LMD machine in making the designed size double-helix HXs. The high speed of the LMD AM process will lead to lower manufacturing cost since the build time of AM components is the most important factor towards the overall AM cost. The high-temperature yet cost-effective AFA alloy may also contribute to the feasibility of LMD AM being a viable mass manufacturing option for CSP HXs, especially for very high-temperature CSP systems.

8. Path Forward:

It is noted that this was a project in the category of Small Innovative Projects in Solar (SIPS), and thus it was exploratory in nature. No technology transfer or commercialization was anticipated for this SIPS project with a small budget and short project duration. The significant accomplishments and conclusions listed in Section 8 will allow future R&D to advance the technology. The AFA alloy has been shown to be easily printable during AM, which will open the door for the alloy to be used in the design of HXs for CSP or other applications. The double-helix design of HXs may find applications and usage in CSP and other areas. Future R&D may include property tests of the AM-printed AFA alloy samples, printing actual HXs and tested at Sandia or other CSP units. Only then, the real-world applications may be approachable.

9. Products:

A presentation was made at technical conferences to provide the research results to the community: Nathan Young, Jess Garnett, Amir Shooshtari, Ji-Cheng Zhao: *Additive manufacturing (AM) of supercritical CO_2 heat exchangers using laser directed energy deposition (L-DED)*. Oral presentation at the *TMS 2025 Annual Meeting & Exhibition*, March 23–27, 2025, Las Vegas, Nevada.

The team also participated at the SETO Merit Review and presented a poster on the results of this project.

No patent disclosures were filed as a result of research under this project and no patents were issued either. The team may write a manuscript for publication in the future.

10. Project Team and Roles:

Dr. Ji-Cheng 'JC' Zhao (PI, Professor): JC served as the overall PI of this project overseeing both the experimental and design parts of the research. He was also responsible for the completion and submission of the quarterly technical reports. Zhao oversaw both technical and programmatic parts of the project.

Dr. Amir Shooshtari (Co-PI, Professor): Amir was a co-PI of this project and led the design of the double helix HX and performed various design iterations based on the experimental input of the particle flow tests.

Dr. Minhua Zhao (Research Scientist): During the early part of this project, Minhua performed preliminary oxide particle flow tests, especially related to using plastic prototypes to determine the minimum gaps and tilt angles to allow the free flow of the oxide particles.

Christian Sanjurjo-Rodriguez (Faculty Specialist): Christian did the early AM work before he took a job at the Applied Physics Laboratory (APL) and before Nathan Young joined the team. Christian was the expert in running and maintaining the TruLaser 3000 AM system.

Mr. Nathan Jay Young (Faculty Specialist): Nathan performed actual additive manufacturing of the coupons and HX prototypes. He maintained and managed the TruLaser 3000 AM system.

Ms. Jessica Garnett (Graduate Student): Jessica performed the geometric design of the plastic HX prototypes that informed the geometric design of the HX. She also performed more accurate measurements of the oxide particle flow tests. Jessica led the 3D printing of the plastic HX prototypes and helped mentor Nandini to do metallographic examination of plates and prototypes of HX made with metal powders using AM. She was also involved in the metal AM process development.

Ms. Nandini Bhattaram (Undergraduate Student): Nandini performed cutting, grinding, polishing, sample preparation and optical imaging to examine the quality of coupons and HX prototypes made using the TruLaser 3000 AM machine. The work is essential to demonstrate the crack-free nature and low-porosity of the AM builds.

11. References:

1. T. Schopphoven, A. Gasser, G. Baskes, EHLA: Extreme high-speed laser material deposition, Laser Tech. J., 14 (4) (2017) 26-29. https://doi.org/10.1002/latj.201700020
2. T. Schopphoven, A. Gasser, K. Wissenbach, R. Poprawe, Investigations on ultra-high-speed laser material deposition as alternative for hard chrome plating and thermal spraying, J. Laser Appl., 28 (2016) 022501. https://doi.org/10.2351/1.4943910
3. T. Schopphoven: Private communication, August 2018.
4. P.J. Maziasz, G. Muralidharan, B.A. Pint, K.A. Unocic, Y. Yang, Low-cost cast creep-resistant austenitic stainless steels that form alumina for high temperature oxidation resistance, US Patent App. 16/510,524, 2019.
5. P.J. Maziasz, G. Muralidharan, B.A. Pint, K.A. Unocic, Y. Yang, Low-cost cast creep-resistant austenitic stainless steels that form alumina for high temperature oxidation resistance, US Patent App. 16/258,526, 2019.
6. Z. Ma, M. Mehos, G. Glatzmaier, B.B. Sakadjian, Development of a concentrating solar power system using fluidized-bed technology for thermal energy conversion and solid particles for thermal energy storage. Energy Procedia, 69 (2015) 1349-59. https://doi.org/10.1016/j.egypro.2015.03.136

7. J.M. Yin, Q.Y. Zheng, X.R. Zhang, Heat transfer model of a particle energy storage-based moving packed bed heat exchanger. Energy Storage. 2 (2020) E113. https://doi.org/10.1002/est2.113
8. K.J. Albrecht, C.K. Ho, Design and operating considerations for a shell-and-plate, moving packed-bed, particle-to-sCO_2 heat exchanger. Solar Energy. 178 (2019) 331-40. https://doi.org/10.1016/j.solener.2018.11.065
9. J.C. Chen, J.R. Grace, M.R. Golriz, Heat transfer in fluidized beds: design methods. Powder Technology. 150 (2) (2005) 123-132. https://doi.org/10.1016/j.powtec.2004.11.035
10. C.K. Ho, High-temperature particle heat exchanger for sCO_2 power cycles (presentation). Sandia National Labs (SNL-NM), Albuquerque, NM (United States); Apr 1, 2016. https://www.osti.gov/servlets/purl/1365201
11. S. Ali, Pressure drop correlations for flow through regular helical coil tubes, J. Fluid Dynamics Res., 28 (2001) 295-310. https://doi.org/10.1016/S0169-5983(00)00034-4.
12. M. Munsch, E. Wycisk, M. Schmidt-Lehr, ***Additive Manufacturing - Make or Buy***, Ampower Insights, vol. 1, October 2017. https://am-power.de/en/insights/cost-additive-manufacturing-make-or-buy-2/
13. K.J. Albrecht, M. L. Bauer, and C.K. Ho*, Parametric analysis of particle CSP system performance and cost to intrinsic particle properties and operating conditions,* ASME 2019 13th International Conference on Energy Sustainability, Paper #: ES2019-3893, 2019. https://doi.org/10.1115/ES2019-3893
14. National Renewable Energy Laboratory. *Concentrating Solar Power Gen3 Demonstration Roadmap*. M. Mehos, G. Turchi, J. Vidal, M. Wagner, Z. Ma, C. Ho, W. Kolb, C. Andraka, and A. Kruizenga. https://www.osti.gov/biblio/1338899